Solar Energy Materials & Solar Cells 218 (2020) 110722

Contents lists available at ScienceDirect

Solar Energy Materials and Solar Cells

journal homepage: http://www.elsevier.com/locate/solmat

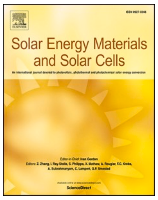

Ge quantum dot lattices in alumina prepared by nitrogen assisted deposition: Structure and photoelectric conversion efficiency

Marija Tkalčević [a], Lovro Basioli [a], Krešimir Salamon [a], Iva Šarić [b,c], Jordi Sancho Parramon [a], Matej Bubaš [a], Iva Bogdanović-Radović [a], Sigrid Bernstorff [d], Zsolt Fogarassy [e], Katalin Balázsi [e], Mladen Petravić [b], Maja Mičetić [a,*]

[a] Ruđer Bošković Institute, Bijenička Cesta 54, 10000, Zagreb, Croatia
[b] University of Rijeka, Radmile Matejčić 2, 51000, Rijeka, Croatia
[c] Center for Micro- and Nanosciences and Technologies, University of Rijeka, Radmile Matejcic 2, 51000, Rijeka, Croatia
[d] Elettra Sincrotrone, S.C.p.A., Strada Statale 14 Km 163.5 in AREA Science Park, 34149Basovizza/Trieste, Italy
[e] Institute of Technical Physics and Materials Science, Centre for Energy Research, Konkoly – Thege M. út 29-33, H-1121, Budapest, Hungary

ARTICLE INFO

Keywords:
Ge QDs
Quantum efficiency
QD lattices
N-assisted deposition
Spectral response
Multiple exciton generation

ABSTRACT

Thin films comprising three dimensional germanium (Ge) quantum dot lattices formed by nitrogen (N) assisted magnetron sputtering deposition in alumina (Al_2O_3) matrix have been studied for light harvesting purposes. In order to expand the application of this material it is necessary to reduce germanium oxidation and to achieve stabilization of the germanium/alumina interface. Effects of tuning the N concentration, substrate temperature and Ge sputtering power during the films preparation are monitored. It is shown that the N presence not only reduces Ge oxidation during annealing but also affects the internal structure, size and arrangement of Ge quantum dots. Additionally, the deposition temperature and Ge sputtering power are used to tune the Ge quantum dot size, separation and the regularity of their positions. It is shown that the optical and electrical properties of the films, especially their photo-induced current, and quantum efficiency are strongly tunable by the deposition conditions. Moreover, a significant photo-response and effect of multiple exciton generation effect is observed. The materials presented could be used as a sensitive layer for photodetectors or photovoltaic light harvesting devices. The presented tools can be used for future fine tuning of the material to achieve the optimal quantum efficiency.

1. Introduction

The control and manipulation of the structure of thin films at the atomic scale has been in the focus of the scientific interest during the past few decades. Semiconductor nanoparticles and quantum dots (QDs) have been studied extensively because of the possibility to tune the band gap by the QD size, generate multiple excitons with a single photon and many other interesting properties which make them an excellent material for the application in photovoltaics and detectors [1–9].

Especially interesting are Ge nanocrystals (NCs) in dielectric matrices and similar low-dimensional structures based on indirect-gap semiconductors [10–12]. Ge has a higher electron and hole mobility than Si, so efforts are being made to study the optical properties of Ge nanostructures and their possible application in photovoltaics [13]. The Bohr exciton radius of Ge (24 nm) is much larger than that of Si (5 nm), causing much stronger confinement effects in Ge NCs. The estimated radiative lifetime of excitons in Ge is also strongly size dependent and varies from nanoseconds to milliseconds corresponding to the diameter of Ge QDs from 1 nm to 3 nm [14]. Ge QDs, annealed in N rich atmosphere, show the possibility to generate multiple excitons after excitation by a single photon [8]. So the materials based on Ge QDs offer many advantages for an application in solar cells and other photo-sensitive devices.

Ge QDs in dielectric matrices are of particular interest due to the numerous possibilities for designing the materials optical and electrical properties due to the very strong quantum confinement effect in Ge, combined with specific properties of the matrix. To ensure the strong confinement in Ge QDs, a matrix with a large bandgap, like alumina (~6.2 eV) should be used [15]. However, oxide matrices cause the oxidation of Ge, which affects strongly the material properties. For

---

* Corresponding author.
E-mail address: maja.micetic@irb.hr (M. Mičetić).

https://doi.org/10.1016/j.solmat.2020.110722
Received 31 January 2020; Received in revised form 30 April 2020; Accepted 26 July 2020

example, the presence of dangling bonds at the Ge/GeO$_2$ interface is a critical issue concerning Ge-based MOSFETs since this interface usually has some defect-related states [16,17].

In our previous work, we have investigated the production conditions of regularly ordered 3D Ge QD lattices in oxide matrices using self-assembling growth by magnetron sputtering [18–21]. These materials have uniformly sized and spaced Ge QDs and show many benefits regarding their structure, including the control of the Ge QDs size and shape. However, the Ge oxidation leads to poor optical and photo-conversion properties of these films. In this work we explore the effects of N addition during deposition of Ge QD lattices in alumina matrix on the Ge oxidation, and consequently on the optical and photo-electric conversion properties of these films. We have shown that the addition of N strongly reduces oxidation of Ge QDs after annealing, so the materials absorption shows tenability by Ge QD size, in accordance with the theoretical prediction. The same effect is well visible in the wavelength dependence of the photon conversion (quantum) efficiency which is found strongly tuneable via the Ge QD size. Moreover, film deposited at 500 °C, with the largest Ge QDs, shows a multiple exciton generation effect, i.e. a quantum efficiency larger than 1. The presented films therefore could be used as a sensitive layer for photodetectors or photovoltaic light harvesting devices.

2. Methods and experimental details

Three series of thin films consisting of 20 alternating Ge and Al$_2$O$_3$ layers were produced by magnetron sputtering deposition (KJLC CMS-18 system) on Si (100) substrate. The Si substrates were cleaned with acetone, isopropyl alcohol and deionized water before loading into the deposition chamber. The substrates were placed on a rotational stage with a rotating rate of 10 rpm. The substrate size was 5×3 cm^2. After the deposition, the substrate was cut into smaller pieces with sizes of approximately 1×1 cm^2, which were used as samples for different measurements. Pure Ge and Al$_2$O$_3$ were used as targets, 3 inch in diameter, in DC (9 W) and RF (250 W) magnetron discharge modes, respectively. The ionized working gas was mostly argon with an admixture of nitrogen. The total pressure (sum of partial pressures of Ar and N$_2$) was kept at the constant value of 3.5 mTorr, during all depositions. The base pressure in the chamber prior the deposition was 10^{-8} mTorr. Details about the deposition parameters of all samples, and the Ge and N atomic percentages in the film, are given in Table 1. After the deposition, the films were annealed in vacuum at 700 °C for 45 min.

The three series of samples differ by: (a) Ge deposition time, (b) N flow rate during the deposition, and (c) deposition temperature. Accordingly, the sample notation is composed of three letters: the first one (L) is related to the thickness of Ge layer (proportional to the Ge deposition time), the second one (N) refers to the N flow rate during the deposition, and the third one (T) is related to the deposition temperature. For each of these parameters three different values are used, so the indices run for 1–3 for all letters.

Table 1
Deposition parameters of the produced Ge QD lattices. F_N–N$_2$ flow rate, T - deposition temperature, t (Ge, Al$_2$O$_3$) - time of deposition of Ge and Al$_2$O$_3$ layers respectively, % Ge - germanium content and % N - nitrogen content (atomic percentage in the film). The atomic percentages for Ge and N were measured by TOF-ERDA after the deposition.

Name/ parameter	F_N/ sccm	T/ °C	t (Ge/Al$_2$O$_3$)/ s	% Ge	% N
L$_1$N$_1$T$_2$	0	400	45/100	11.7 ± 0.7	0.71 ± 0.09
L$_1$N$_2$T$_2$	2	400	45/100	12.7 ± 0.8	2.1 ± 0.2
L$_1$N$_3$T$_2$	5	400	45/100	12.8 ± 0.8	6.0 ± 0.4
L$_1$N$_2$T$_1$	2	300	45/100	12.1 ± 0.8	2.6 ± 0.2
L$_1$N$_2$T$_3$	2	500	45/100	13.8 ± 0.9	2.0 ± 0.2
L$_2$N$_2$T$_2$	2	400	65/100	16 ± 1	2.9 ± 0.2
L$_3$N$_2$T$_2$	2	400	85/100	20 ± 1	2.9 ± 0.2

High Resolution Transmission Electron Microscopy (HRTEM) investigations were carried out in an aberration corrected THEMIS microscope at 200 keV. Formed Ge QDs were also observed using a high angle angular dark-field detector (HAADF) in scanning transmission electron mode (STEM). For the Energy Dispersive Spectroscopy (EDS) mapping a Super-X detector was used. The cross-sectional TEM samples were prepared by conventional Ar ion beam milling.

The elemental composition of the samples, shown in Table 1, was measured by Time-of-flight Elastic Recoil Detection Analysis (TOF-ERDA). The measurements were done using a 20 MeV ^{127}I^{6+} beam, the angle between sample surface and beam was 20°, and the spectrometer was placed at 37.5°.

A powerful method for statistical structure analysis is Grazing Incidence Small Angle X-ray Scattering (GISAXS) and Grazing Incidence Wide Angle X-ray Scattering (GIWAXS). GISAXS is used complementally with microscopy and provides data collected from a large amount of nanoparticles ($\sim 10^{12}$) so it ensures statistical relevance of the results, which is important for QD lattices since their ordering regularity can significantly vary. These measurements were made at the synchrotron Elettra (Trieste, Italy) using a photon energy of 8 keV. The scattered radiation was collected simultaneously by a two-dimensional Pilatus3 1 M detector (GISAXS) and a two-dimensional Pilatus 100 k detector (GIWAXS). The grazing incidence angle was slightly above the critical angle for total reflection.

XRD measurements were performed using a D5000 thin film diffractometer under the grazing incidence angle of 0.4 deg.

The oxidation of Ge in all samples was determined by X-ray photoemission spectroscopy (XPS) in a SPECS XPS instrument equipped with a hemispherical electron analyser and monochromatized Al Kα X-rays of 1486.74 eV. The photoemission spectra were taken around the Ge 2p core levels and simulated with mixed Gaussian-Lorentzian functions with Shirley background subtraction. The binding energy scale was calibrated against the position of the C 1s peak placed at 284.5 eV.

Spectroscopic Ellipsometry (SE) measurements were carried out with a V-VASE ellipsometer (J.A. Woollam) in the range between 0.5 and 5 eV at an angle of incidence of 70°. Modelling of the ellipsometric measurements was carried out by considering the Ge QDs in Al$_2$O$_3$ composite film as a single homogenous layer. The photon energy dependence of Ge–Al$_2$O$_3$ layer effective optical constants was represented by a sum of Gaussian oscillators, due to its flexibility in modelling multi-component systems. The Ge–Al$_2$O$_3$ layer thickness was fixed to the values obtained by GISAXS measurements. For several annealed samples a thin layer of surface roughness, modelled with the Bruggeman effective medium approximation with 50% Ge–Al$_2$O$_3$ and 50% void, was added on the top of the Ge–Al$_2$O$_3$ film to obtain satisfactory data fitting. Since sputtered alumina has an optical band gap around 6.2 eV, it is transparent in the visible spectrum [22]. Therefore, photon absorption revealed by the imaginary part of the dielectric function can be associated to Ge QDs in the measurements spectral range.

For the current-voltage (I–V) and quantum efficiency (QE) measurements, we have used a Photovoltaic Testing System – Spectral Response and Quantum Efficiency from Sciencetech, (White Light Quantum Efficiency System), in the spectral range from 320 nm to 1200 nm using a bias voltage of 5 V. The I–V measurements were taken upon illumination of the samples with 1 sun (100 mW/cm^2), obtained by a 150 W Xenon lamp and an AM1.5G filter.

For the electrical measurements, the films were coated by an indium tin oxide (ITO) layer on the film surface to serve as an optically transparent contact, and an Al thin layer on the bottom side of the Si substrate. Both contacts were deposited using the same sputtering system as used for the films deposition. Deposition was performed at room temperature, resulting in the thickness of both contacts of approximately

100 nm. 4 square-like top contacts were deposited, each of them covering 9 mm^2 of the surface, and a single back contact covering approximately 30 mm^2 of the surface. The testing of the electrical properties was performed for all 4 front contacts, and the mean value was taken.

3. Structural properties

3.1. Quantum dot self-assembly

The ordering of Ge QDs in alumina is investigated by a combination of the TEM and GISAXS techniques. TEM provides information in real space, while GISAXS shows the structural properties in reciprocal space with excellent statistics, and it is very suitable for the precise characterization of the regularity in the QD ordering. Using on adequate GISAXS analysis procedure it is possible to obtain values for the QD shape, average size, ordering properties and the statistical distribution of all mentioned parameters. GISAXS maps of the investigated films are shown in Fig. 1. All maps show horizontal sheets, centred at $Q_y = 0$ nm^{-1}, and clearly visible peaks with the centre at approximately $Q_y = \pm 1$ nm^{-1}. The horizontal sheets are related to the multilayer structure of the films, while the side peaks show the presence of 3D regularity in the QD positions. These peaks, therefore, are of particular interest for the analysis as they reveal the quality of the self-assembled growth. So, all films show 3D ordering of the Ge QDs, however, the quality of ordering as well as the QD sizes depend on the deposition conditions.

All structural parameters are obtained by numerical analysis of the GISAXS maps [21]. We assume that the Ge QDs are arranged in a body tetragonal lattice characterized by the basis vectors $\boldsymbol{a}_1$-$\boldsymbol{a}_3$. Vectors $\boldsymbol{a}_1$ and $\boldsymbol{a}^2$ are placed in the plane parallel to the substrate (assumed x-y plane), while the third basis vector $\boldsymbol{a}_3$ defines the vertical ordering of the QDs. The separations between QDs are equal in the plane parallel to the substrate, so $|\boldsymbol{a}_1| = |\boldsymbol{a}_2| = a$, while the vertical ($z$) component of $\boldsymbol{a}_3$ equals multilayer period c. The shape of the QDs is assumed to be spheroidal with the radius R_L in the plane parallel to the surface, and R_V perpendicular to it. Details about the determination of structural parameters from GISAXS can be found in Ref. [21], while Table 2 summarizes the main parameters obtained from the fits: in-layer dot separation a, multilayer period c, deviations of the QD positions from the ideal ones ($\sigma^{xy}_{1,2}$, σ^{xy}_{3}, $\sigma^{z}_{1\text{-}3}$), QD radii (R_L and R_V) and the standard deviation of their distribution σ_R. The GISAXS maps of the films annealed at 700 °C are practically the same as from the as-grown ones. Two examples are shown in the insets of Fig. 1(f)-(i). This is in agreement with our previous results, showing that the disintegration of the films starts at 800 °C [20].

Self-organized growth of Ge QDs in alumina is regarded as a combination of diffusion-mediated nucleation and enhanced nucleation probability in the troughs of the underlying substrate. If diffusion-mediated nucleation would be the only growth mechanism of Ge QDs there would be only in-layer spatially correlated QDs, with no interlayer correlations. Since the nucleation is more probable in the troughs of the previous layer, there should be a correlation in the QD position between

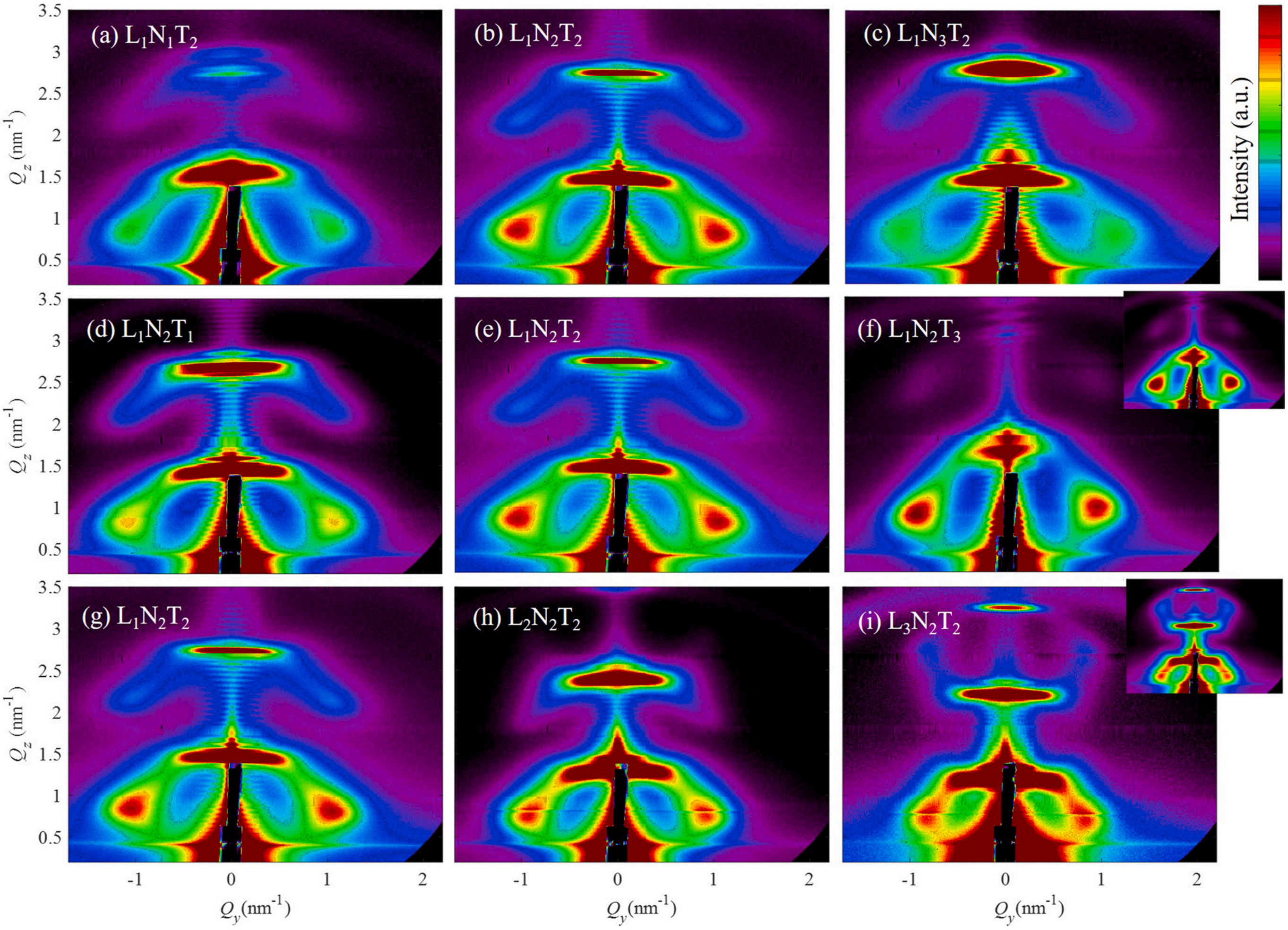

Fig. 1. GISAXS maps of the films. (a)–(c) nitrogen content is increasing, (d)–(f) deposition temperature is increasing and (g)–(e) Ge layer thickness is increasing. The GISAXS maps of the annealed films are practically the same as the non-annealed. Two examples are shown in the insets of the panels (f) and (i).

Table 2

Parameters of the Ge QD array determined by fitting their GISAXS maps shown in Fig. 1. All values are given in nm.

name/parameter	A	C	$\sigma_{1,2}^{xy}$	σ_3^{xy}	$\sigma_{1\text{-}3}^{z}$	R_L	R_V	σ_R
$L_1N_1T_2$	5.3	4.2	1.5	0.9	0.5	1.4	0.9	0.4
$L_1N_2T_2$	5.2	4.1	1.5	0.7	0.1	1.5	0.9	0.4
$L_1N_3T_2$	5.2	4.1	1.6	0.8	0.3	1.1	0.9	0.3
$L_1N_2T_1$	5.3	4.5	1.5	0.9	0.4	1.2	0.8	0.3
$L_1N_2T_3$	6.0	3.4	1.6	0.8	0.4	2.1	1.7	0.4
$L_2N_2T_2$	6.1	4.2	1.5	0.9	0.7	2.0	1.6	0.4
$L_3N_2T_2$	6.2	4.3	1.6	0.9	0.8	3.1	1.7	0.5

$a = |\boldsymbol{a}_1| = |\boldsymbol{a}_2|$ -in-layer dot separation.
$c = |\boldsymbol{a}_3^z|$-multilayer period.
$\sigma_{1,2}$. this should be in te same line with the 'xy'
^{xy}, σ_3^{xy}, $\sigma_{1\text{-}3}^{z}$-deviations of the QD positions from the ideal ones defined by basis vectors $\boldsymbol{a}_1$-$\boldsymbol{a}_3$.
R_L and R_V -QD radii and the standard deviation of their distribution σ_R.

the layers, as explained in detail in Refs. [20–23].

From the results obtained by GISAXS analysis we can see three important properties of the deposition process. They are shown in Fig. 2. First, the addition of nitrogen (N_1–N_3) to the working gas during deposition does not influence significantly the deposition rate of Ge. Therefore, the film thicknesses, as well as the QD lattice parameters are nearly the same, despite the change of the nitrogen partial pressure (the total pressure was kept constant). However, the nitrogen influences the ordering quality of the Ge QDs. The second order of Bragg spots are narrower and more visible for the film with 2% nitrogen ($L_1N_2T_2$). The same follows from the numerical analysis of GISAXS, parameters $\sigma_3^{x,y}$ and $\sigma_{1\text{-}3}^{z}$ (see Table 2). Second, the increase in the deposition temperature (T_1-T_3) results in larger Ge QDs. A more significant effect is on the lateral radius of the Ge QDs, R_L, as it increases from 11.9 nm to 20.8 nm when the deposition temperature changes from 300 °C to 500 °C. Therefore, the deposition temperature can be used to control the lateral size of QDs. Finally, the thickness of the Ge layer (L_1-L_3) influences mostly the vertical radius, R_v, of Ge QDs, since it changes from 8.3 to 25.9 nm for the Ge layer deposition times 45 s–85 s. However, the lateral Ge QD size also increases and the QDs overlap for the highest Ge layer thickness, so actually we get continuous layer of Ge, not separated QDs.

Thus, the nitrogen content, deposition temperature and Ge layer thickness are important deposition parameters that allow us to control the size and separation of Ge QDs and their ordering quality. It will be shown in the following sections that these properties significantly affect the optical and photo-electrical properties of the materials, so their control can be a powerful tool for optimizing photoelectric and photovoltaic devices.

The incorporation of nitrogen during the magnetron deposition process implies possible changes in the dynamics of the plasma, since with increasing number of nitrogen molecules there is a greater probability for collisions. More collisions promote dissociation of N_2 and provide in this way a continuous source of atomic nitrogen [24]. It has also been shown that increasing the nitrogen flow continuously decreases the thickness of the film as well as the crystallinity. Furthermore, an increasing nitrogen flow rate seems to have a big effect on the grain size [25,26].

TEM measurements of the film $L_1N_2T_3$ are shown in Fig. 3. The figure shows the formation of ellipsoidal Ge QDs with lateral and vertical sizes of about 4 nm and 3 nm, respectively, which is in excellent agreement with the results of the GISAXS analysis. The elemental composition of the films, shown in Fig. 3(b), is in agreement with the formation of Ge QDs in alumina matrix. The Si substrate native oxide is also well visible. It has a thickness of about 2.5 nm. Together with the alumina oxide layer of similar thickness, it represents a potential barrier for the carriers from the Si substrate.

3.2. Ge QD internal structure

The internal (crystalline) structure of the films, measured by the diffraction technique, is demonstrated in Fig. 4. XRD patterns for all as deposited samples show two broad maxima centred at ~27 deg and ~48 deg (Fig. 4(a)–(c)), revealing an amorphous nature of the Ge QDs in the as deposited films. Interestingly, it is noticeable how the degree of short-range ordering of Ge atoms varies with the deposition conditions, as suggested by the relative intensity of the second maximum at ~48 deg. This maximum gets more suppressed with more N within the film, indicating that the presence of nitrogen further decreases the degree of spatial ordering of Ge atoms. The degree of local atomic ordering also depends on the Ge layer thickness (Fig. 4(c)): it increases with the thickness which can be related to the concurrent increase in size of Ge QDs, while it does not depend significantly on the deposition temperature (Fig. 4(b)).

The diffractograms of the annealed films (Fig. 4(d)–(f)) match with the simulated XRD spectra of Ge nanocrystals (crystallites) (shown by dashed lines at the bottom), revealing crystallization of Ge QDs during annealing. A small shift of the reflection positions is visible in the measured curves indicating the presence of stress in the formed QDs causing smaller lattice constants than in the bulk Ge. This effect has already been investigated in Ge QDs in alumina matrix [20]. The size of the formed Ge crystallites is estimated from the FWHM of the Ge (111) reflection using the Scherrer formula. This method does not yield accurate sizes, but we take the trend of the change in the crystallite size as reliable. These trends are shown in the insets of Fig. 4(d)–(f) for the three varied deposition parameters. First we note that the sizes of the formed Ge crystallites are significantly smaller than the sizes of the Ge QDs found by GISAXS analysis (see Table 2). This indicates that, after annealing the Ge quantum dot consist of several smaller crystallites. In

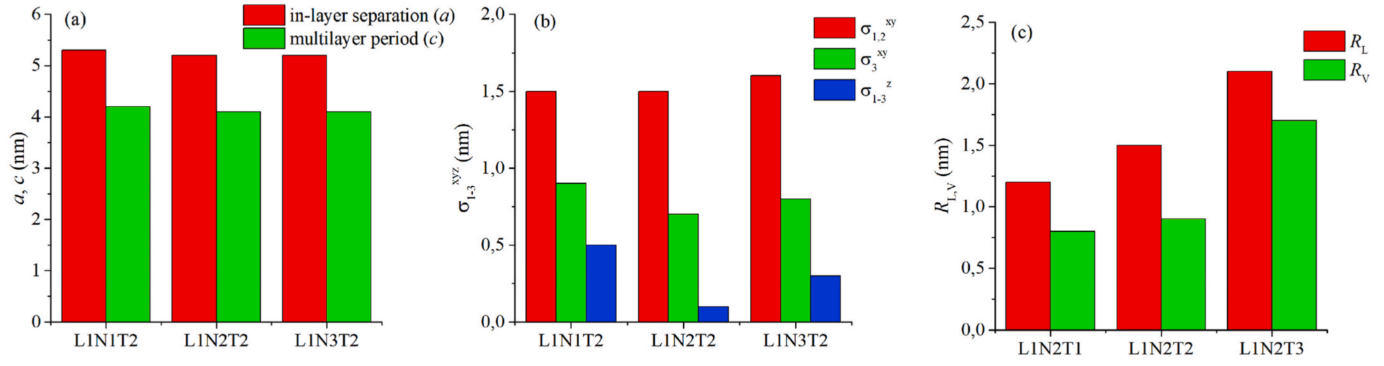

Fig. 2. Bar plots of the main structural parameters of the films. (a) In layer separation a of the Ge QDs, and the multilayer period c in dependence on the N concentration. (b) Disorder parameters $\sigma_{1\text{-}3}{}^{xyz}$ in dependence on the N concentration. (c) Lateral and vertical radii (R_L and R_V) in dependence on the deposition temperature.

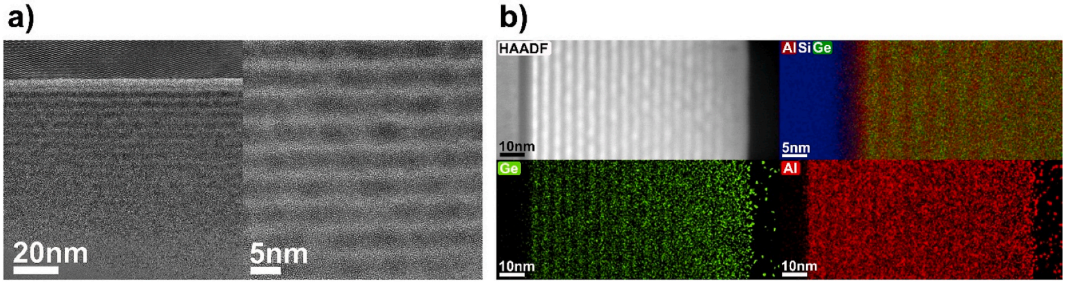

Fig. 3. TEM images of $L_1N_2T_3$ film. (a) HRTEM images with different magnifications, (b) (HAADF-STEM) image together with EDS coloured elemental maps.

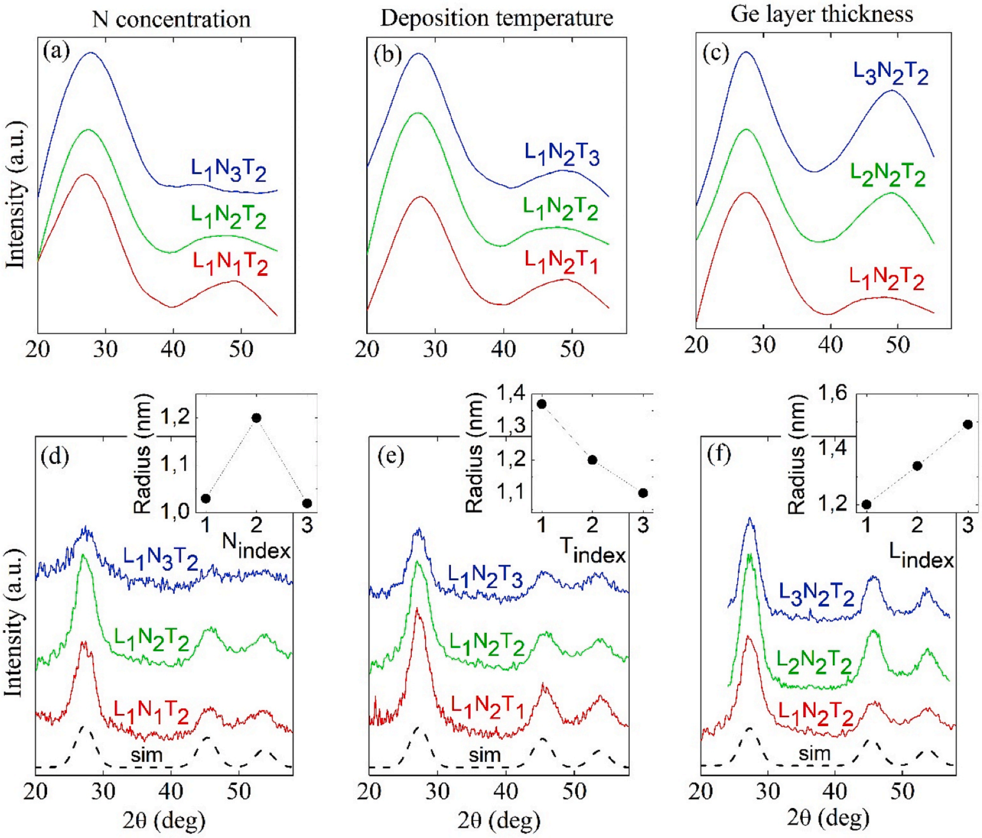

Fig. 4. XRD spectra of all samples after (a)–(c) deposition and (d)–(f) annealing in vacuum for 45 min. The simulated curves of crystalline Ge QDs are shown by dashed lines. The insets show the *c*-Ge QD radii obtained from the fitting of the corresponding diffraction curves. The X-axis in the insets indicates the number of the changing index in the sample name for each series.

addition, the crystallite size and the whole Ge QD size shows opposite trends (Fig. 4(e) and Table 2). This suggests that a higher deposition temperature, in combination with the presence of nitrogen, results in more crystallization centres within the QDs, as observed previously [25,26]. The Ge crystal size increases with the Ge-layer thickness as expected and found by GISAXS analysis.

3.3. Germanium oxidation

The formation of Ge–O bonds and the oxidation states of Ge can be determined from the chemical shifts in XPS spectra taken around the Ge 2p and O 1s core levels. We focus here on the Ge 2p photoemission as it shows larger chemical shifts and a more distinctive structure than O 1s (Ref. [19,27]). The representative spectra from the selected films prepared with three different concentrations of nitrogen ($L_1N_1T_2$, $L_1N_2T_2$ and $L_1N_3T_2$) are shown in Fig. 5. Before the XPS analysis, the samples were slightly etched by 2 keV Ar^+ bombardment within the analysis chamber to remove surface contamination (sputtering off approximately 2 nm from the film surface). In general, the ion bombardment of semiconductor surfaces, used as a method of surface preparation (surface cleaning or ion-assisted etching) can create some damage in the near-surface region, including implantation of Ar ions, preferential sputtering, cascade mixing, and amorphization, or even changes in the electronic structure, all of which can influence the XPS data interpretation. The ion-induced damage was minimized in the present study by the use of relatively low energy and bombardment time of Ar^+ ions, resulting in no detectable changes in the XPS spectra.

The Ge 2p photoemission is characterized by the large spin-orbit splitting of the $2p_{3/2}$ and $2p_{1/2}$ levels while in Fig. 5 we show only the part of the spectra around Ge $2p_{3/2}$. From the fitting of the experimental curves, we note that, in addition to metallic Ge (Ge (0)), Ge is oxidised in all samples mostly in the +4 oxidation state (GeO_2). The first two films with 0% and 2% of N, respectively (Fig. 5(a) and (b)) have a similar ratio of Ge (0) and Ge oxides. The third film has a significantly larger amount

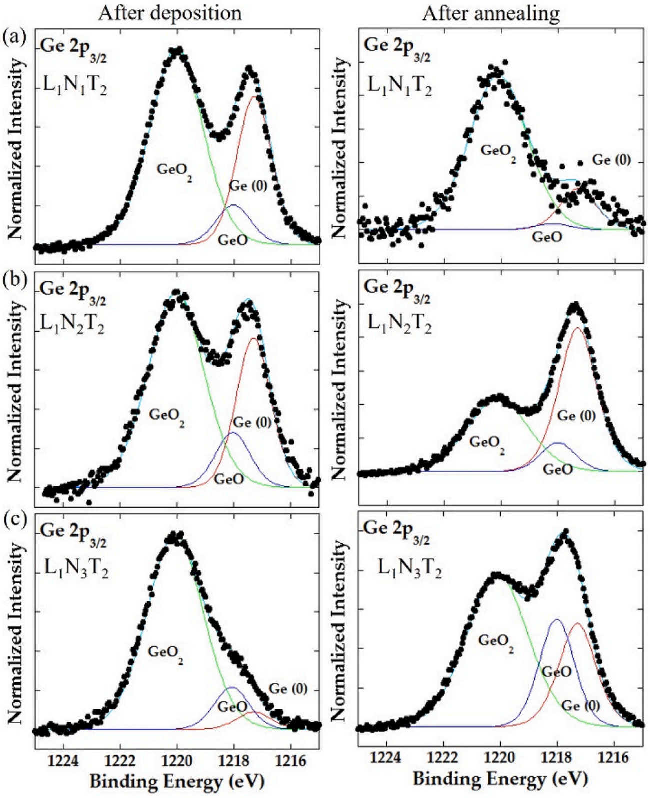

Fig. 5. XPS measurements of the $L_1N_1T_2$, $L_1N_2T_2$ and $L_1N_3T_2$ films after deposition (left) and after annealing (right).

of oxide, but that film also has the smallest Ge QDs (larger dot surface per unit volume ratio, providing a larger oxidation area). From these measurements we conclude that the presence of N during the deposition does not influence significantly the formation of Ge oxides. The most interesting results of the XPS measurements are obtained on the same films after annealing as shown in the right column of Fig. 4. The annealed films with N (Fig. 5(b) and (c)) show a significant reduction of oxides with the amount of nitrogen. Although the oxide has not been completely removed by annealing, this result could be an important guideline for the preparation of oxide–free Ge QDs. A similar observation was found in Ref. [28] where a stabilization of the GeO_2/Ge interface by N addition was demonstrated.

4. Optical properties

Fig. 6 shows the dependence of the imaginary part ε_2 of the films dielectric function on the photon energy, closely related to the absorption of the films, obtained from the ellipsometry measurements. The measurements show a strong dependence on the deposition conditions and on the annealing treatment. Fig. 6(a)–(c) show the spectra of the films before annealing, while the annealed ones are shown in Fig. 6(d)–(f).

First we consider the ε_2 of the non-annealed films. Although the QD sizes and their separations are very similar for the first series of the films differing by the N amount ($L_1N_{1\text{-}3}T_2$), as well as the Ge atomic percentage, their curves differ significantly. The first two spectra (N_1 and N_2) are similar, they both have a relatively sharp double peak, with the maxima close to 3.5 eV and 3.8 eV, superimposed on a broader signal. The third spectrum (highest N content) has a lower signal with no sharp peaks. That film has practically no second Ge diffraction peak (Fig. 4(a)) and shows the highest relative amount of GeO_2 (Fig. 5(c)).

The second series, differing by the deposition temperature ($L_1N_2T_{1\text{-}3}$), again shows similar features for the first two films, while the third one, deposited at the highest temperature, is again lower in the intensity

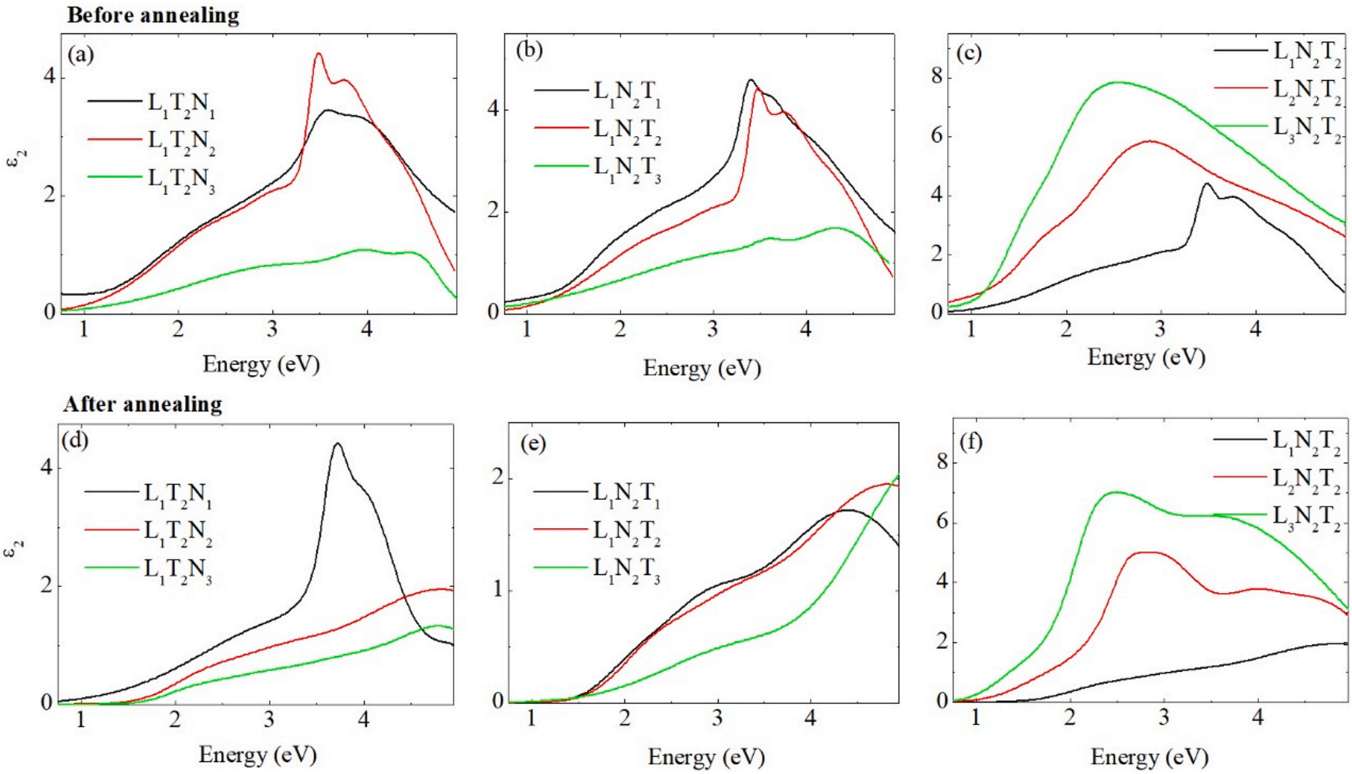

Fig. 6. Imaginary part of the dielectric function determined by ellipsometry measurements for all investigated films (a)–(c) before and (d)–(f) after annealing treatment.

and with no sharp peaks. Although the last film shows similar optical properties as the one with the highest N content from the first series, this film shows the presence of the second diffraction Ge peak (Fig. 4(b)).

The third series differing by Ge layer thickness ($L_{1\text{-}3}N_2T_2$), shows the sharp peaks only for the thinnest Ge layers (L_1). The overall intensity of the other two films increases with Ge–layer thickness and the peak position shifts toward smaller energies. All of these films show a well-developed second peak in the diffraction curves.

Considering all above, it seems that the appearance of the sharp peaks is not related to the crystalline structure of Ge, but most probably it is related to the presence of Ge oxide. In order to understand better all the features, we analyse the spectra of the annealed films shown in Fig. 6 (d)–(f). It is interesting that the sharp intense peaks disappeared for all annealed films except the one with no N addition (Fig. 6(d)). According to the XPS analysis, the relative amount of Ge oxide increases after annealing only for that film, while in all films with addition of N, the amount of GeO_2 decreases. Therefore, we believe that the strong peaks are related to the presence of GeO_2 around the Ge QDs. However, according to the data from the literature, GeO_2 should not have some intense peaks in that energy range [28], so it is very possible that the features are related to some specific structure forming at the Ge/GeO_2 interface [29], and/or to the modification of the Ge properties due to the GeO_2 shell. Alumina matrix has a very low absorption in this energy range so we do not take it into account [30]. In our previous work we have shown that the presence of a Si shell around Ge can significantly influence their optical properties [31,32] also showing that sharp features in their absorption spectra become enhanced when the shell-to-core radius ratio increases. Thus, the formation of a GeO_2 shell around a Ge core could affect the absorption curves of the QDs.

Finally, we consider the position of the peaks in the ε_2 of N-containing films after annealing in Fig. 6(d)–(f). These peaks are broader than the previously considered ones, but their positions strongly depend on the deposition conditions. It is interesting that the positions show a correlation with the sizes of crystalline Ge QDs as demonstrated in the insets of Fig. 4(d)–(f). When the crystal size decreases, the peak position shifts toward higher energies, which is well visible in Fig. 6(e). The opposite shift is visible if the crystallite size increases, as demonstrated in Fig. 5(f). These shifts are in accordance with the confinement theory and the size-dependent Ge bandgap. The energy positions of the peaks are close to the theoretical values, with a small extra shift toward larger energies [20,33].

We conclude that the absorptions of the as-grown films and the film with no N added are strongly influenced by the presence of Ge oxide around the Ge QDs. It causes the appearance of strong and sharp absorption peaks, with approximately the same energy position. The annealed films, which were prepared with the presence of N, show broader peaks with the positions strongly dependent on the *c*-Ge size, in accordance with the confinement theory for Ge nanocrystals.

5. Photo-response

Photo-current and electrical properties were measured by contact geometry as described in section 2. Typical I–V measurements of the as-grown and annealed films are shown in Fig. 7, together with the scheme of the geometry used for the measurements. It is clear from the measurements that light enhances the current in both cases (before and after annealing). However, the photo-generated current is more than 100 times stronger for the same film after annealing. The reason of such current improvement is double. The first one is a strong reduction of Ge oxidation by annealing as shown by the XPS measurements. The second reason is a strong decrease of the defects number by annealing as the Ge QDs crystallize. A similar effect was observed by other authors [34,35]. All films show a similar behaviour. Therefore, we shall consider only the annealed films in the further analysis.

The photo-electrical properties of all annealed films are shown in Fig. 8. The dependence of the current on the applied voltage is shown in Fig. 7(a)–(c). The strongest photo-current is generated for the middle-amount of nitrogen ($L_1N_2T_2$, see Fig. 8(a)), similarly to the imaginary part of the dielectric function. The comparison of currents from films deposited at different temperatures is shown in Fig. 8(b). The strongest current is generated in the film deposited at the highest temperature ($L_1N_2T_3$). This film is also characterized by the strongest current obtained from all investigated films. The dependence of the current on the Ge–layer thickness (Fig. 8(c)) shows the opposite trend. An increase in the layer thickness with the corresponding increase of the amount of Ge causes a decrease in the photo-generated current. The films are not prepared in the solar cell configuration, so the values of the open circuit voltage and the short circuit current are close to zero.

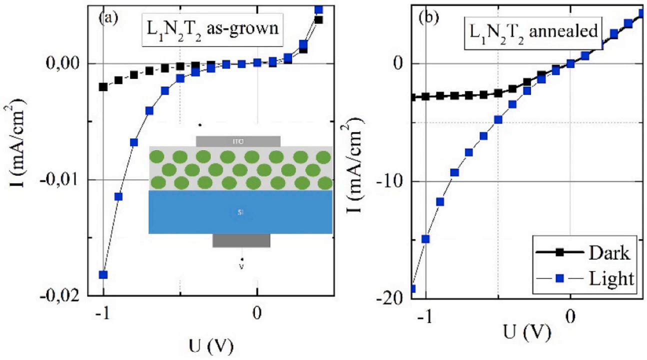

Fig. 7. I–V curves of the (a) as-grown and (b) annealed film $L_1N_2T_2$. The scheme of the geometry for the measurement is shown in the inset of panel (a).

The difference between the photo-generated and dark current for all films at a bias voltage of 1.8 V is demonstrated in Fig. 8(d)–(f). As discussed before, the result of an increased deposition temperature is an increase of the photo-generated current, while an increase in the Ge-layer thickness causes a decrease of the current. The number of photo-generated carriers is related to the materials properties, i.e. the opposite trend with respect to the Ge crystallite size. The reason of such behaviour is further explored by measurement of the quantum efficiency (QE).

The photo-generated current show relatively small fill-factor. To understand better such behaviour, we have determined the resistance and shunt resistances from the dark current measurements, according to the procedure described in Ref. [36]. The obtained values are plotted in Fig. 8(g)–(i). The general property of the resistances is that they are high for the small values of the photo-generated currents (please compare the panels (d)-(f) and (g)–(i) in Fig. 8). The shunt resistances are in the range of kΩ, so they should not alter much the photo-generated current. However, the series resistances are quite high for most of the films, and they very probably reduce the fill-factor. Such behaviour is probably caused by strongly isolating alumina matrix, and large separation of Ge QDs.

The dependence of the photo-generated current on the light energy is shown in Fig. 9. The curves represent the QE, i.e. the number of extracted electron-hole pairs per one incident photon. The arrows indicate the positions of the bandgaps for the Ge QDs as determined from the structural parameters, all of them given in Table 3. From the measurements follows that the QE strongly depends on the films preparation conditions.

The influence of N addition on the QE is shown in Fig. 9(a). The best efficiency is obtained for the middle N concentration, in accordance with the I–V measurements shown in Fig. 8(a) and (d). The positions of the peaks in the QE correspond roughly to the Ge QD bandgap values for the films containing nitrogen, ($L_1N_2T_2$ and $L_1N_3T_2$). The film without nitrogen, $L_1N_1T_2$, does not show a matching of the maximum of the QE curve and the bandgap values, which is probably a consequence of oxide formation. The same film showed different optical properties caused by the same reason (see Fig. 6).

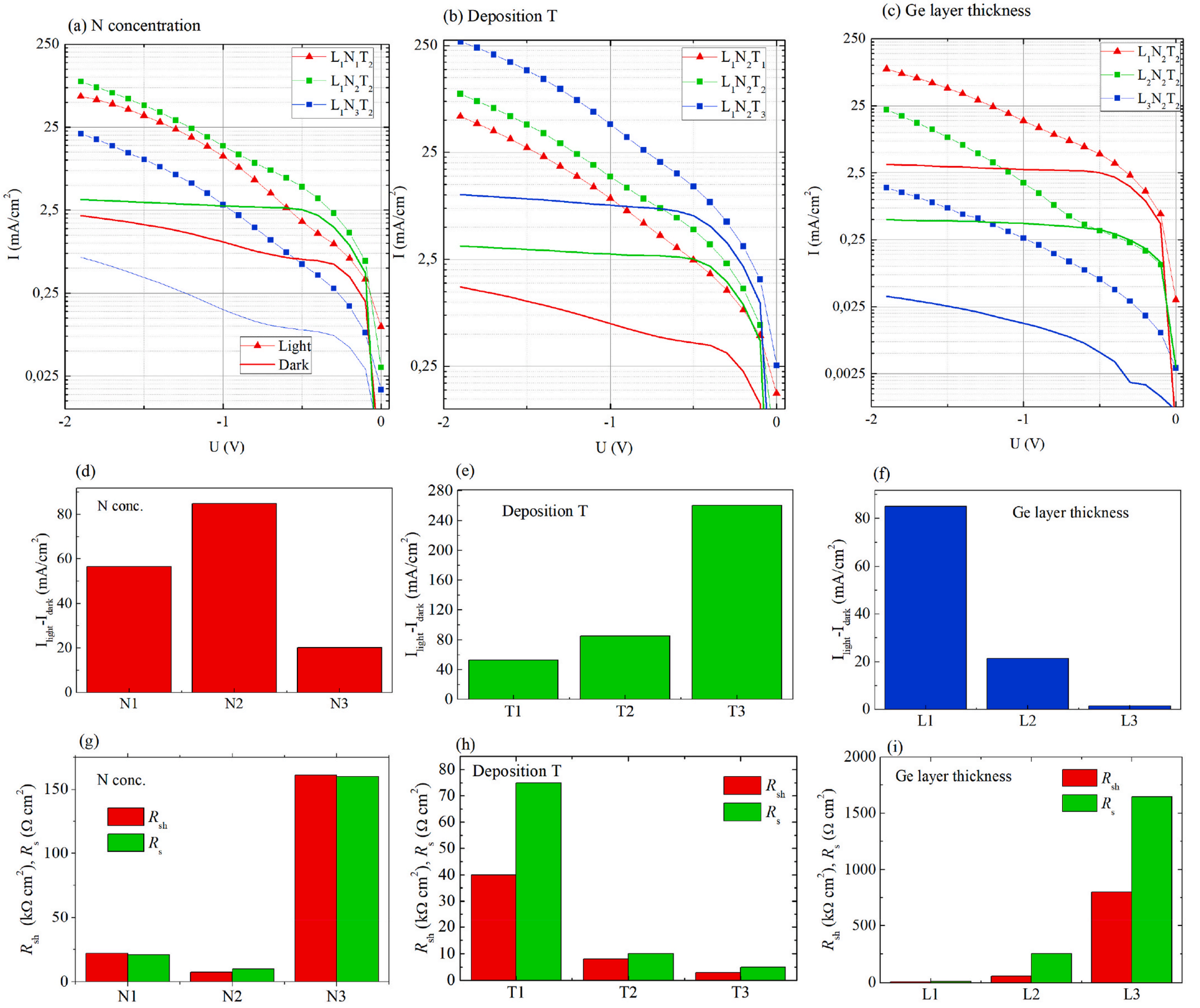

Fig. 8. (a)–(c) I–V curves of the annealed films for a bias voltage between 0 and 2 V, (d)-(f) difference between current generated in dark and light at a bias voltage of 1.8 V for three series of the films. (g)-(i) Shunt and serial resistances (*R*sh and *R*s respectively), determined from the dark current measurements.

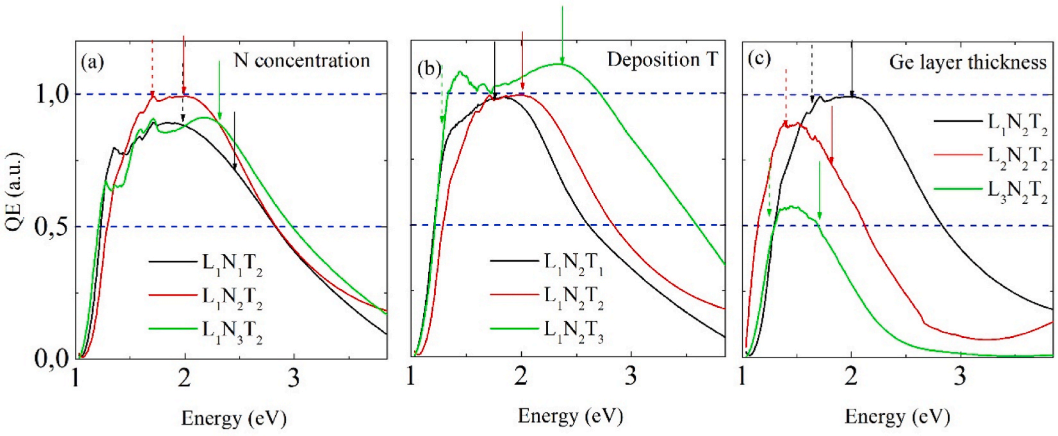

Fig. 9. Quantum efficiency (number of generated electron-hole pairs per photon) for all investigated films after annealing. The arrows indicate the positions of the bandgap calculated from the radius of the Ge QDs (dashed arrow) and the Ge crystallite size (full-line arrow), see Table 3. The colour of the arrows corresponds to the colour of the QE lines of the same film. (For interpretation of the references to colour in this figure legend, the reader is referred to the Web version of this article.)

Table 3
Parameters of the Ge QD sizes (R_{QD}, R_{cryst}) and bandgap values ($E^G{}_{QD}$, $E^G{}_{cryst}$) obtained from the Ge size determined from the GISAXS and XRD measurements respectively, according to the theory given in Ref. [12].

name/parameter	R_{QD} (nm)	$E^G{}_{QD}$ (eV)	R_{cryst} (nm)	$E^G{}_{cryst}$ (eV)
$L_1N_1T_2$	1.2	2.0	1.05	2.3
$L_1N_2T_2$	1.3	1.9	1.2	2.0
L_1N_3T2	1.1	2.3	1.1	2.3
$L_1N_2T_1$	1.4	1.8	1.4	1.8
$L_1N_2T_3$	2.0	1.3	1.1	2.3
$L_2N_2T_2$	1.9	1.4	1.4	1.8
$L_3N_2T_2$	2.5	1.2	1.5	1.7

The deposition temperature dependence of the QE (Fig. 9(b)) shows two interesting features. The first one is its dependence on the Ge nanocrystal radius. The QE curve is shifting toward larger energies with decreasing Ge crystalline size (see Fig. 4(c)), which is in agreement with the confinement effect in Ge crystals. The positions of the bandgaps correspond to the maxima of the QE curves, as visible from the positions of the arrows. The second very interesting property is the value of QE which is larger than 1, measured for the film grown at the highest temperature ($L_2N_2T_3$). The same film also has the highest photo generated current (around 3 times larger than the second one), as discussed earlier (Fig. 8(d)–(f)). The position of the QE peak with the intensity larger than 1 is around 2.5 eV. This value should be two times the Ge QD bandgap value, if two exciton generation caused its appearance. The value of the bandgap for this film should be around 1.3 eV according to the size of the Ge QDs for this film, which is around 4 nm (see Table 3 and Refs. [6,12]). This indicates strongly that the observed effect is indeed the consequence of two exciton generation after single photon excitation. The same film also shows a much stronger QE at energies larger than 3 eV than all other films. We believe that three exciton generation (expected at the energies 3.5–4.0 eV) also occurs and rises the QE at larger energies. It is not clear the influence of Ge QD and Ge crystallite size. These two parameters show the opposite trends with the deposition temperature increase. It seems that both of them have an influence on the photo-electric properties. The crystalline size on the optical, and the QD size on the photo-electrical.

Finally, the effect of the Ge layer thickness i.e. the Ge QD size is demonstrated in Fig. 9(c). A clear shift toward smaller energies with the Ge QD size is evidenced, as well as a decrease of the overall QE. Increasing the Ge layer thickness, the Ge QDs become larger and they start to touch each other, as discussed in the section of the GISAXS measurements, causing the appearance of many defects at their boundaries. Additionally, the confinement effects decrease, as the QDs are not surrounded by the high-bandgap matrix. They form a 2D system instead. Therefore, the observed energy shift toward smaller energies is expected in accordance with the formation of 2D Ge layer and of course by increasing of the Ge QDs size. The decrease of the intensity is probably caused by the increased number of defects in germanium, which form at the Ge crystallite grain boundaries for high Ge layer thicknesses which causes Ge QD overlapping. The larger number of defects causes an increased recombination of carriers within these layers, and a smaller spectral response as well as a smaller photocurrent, as visible from Fig. 8 (c) and (f).

In summary, all QE measurements are in accordance with the I–V measurements and the number of photo-generated carriers.

6. Conclusions

We have investigated the effect of nitrogen addition during magnetron sputtering deposition of materials consisting of 3D-ordered Ge quantum dots embedded in an alumina matrix on their structural, light absorption and photo conversion properties. We have shown that the addition of N strongly affects the material optical and photo-generation properties, while it does not affect significantly the self-assembled growth of Ge quantum dots and formation of 3D ordered Ge quantum dot lattices. The addition of N reduces oxidation of the Ge quantum dots, so the effects of quantum confinement are clearly visible in their optical properties. The optimal conditions for photo-induced current are explored, and it is shown that higher deposition temperatures and thinner Ge layers leading to the formation of isolated Ge quantum dots, improve the photo-induced current. The material produced at the highest temperature (500 °C) shows the effect of multiple exciton generation, while the quantum efficiency of all materials deposited with N assistance shows a peak corresponding to the bandgap of the Ge quantum dots. The above mentioned effects and the material itself could be very useful in light harvesting and the production of heavy–metal free high-efficient solar cells and photodetectors.

CRediT authorship contribution statement

Marija Tkalčević: QE measurements, Writing - original draft. **Lovro Basioli:** GISAXS measurements and data processing; electrical measurements. **Krešimir Salamon:** XRD measurements and data processing. **Iva Šarić:** and. **Jordi Sancho Parramon:** ellipsometric measurements and data processing. **Matej Bubaš:** ellipsometric measurements and data processing. **Iva Bogdanović-Radović:** TOF-ERDA measurements and data processing, Writing - original draft. **Sigrid Bernstorff:** GISAXS measurements, Writing - review & editing. **Zsolt Fogarassy:** TEM measurements and data processing. **Katalin Balázsi:** TEM measurements and data processing. **Mladen Petravić:** XPS measurements and data processing. **Maja Mičetić:** Conceptualization, Methodology, Software, for GISAXS analysis, Writing - original draft, Writing - review & editing.

Declaration of competing interest

The authors declare that they have no known competing financial interests or personal relationships that could have appeared to influence the work reported in this paper.

Acknowledgements

This work has been partially supported by the European Regional Development Fund (ERDF) under the (IRI) project "Improvement of solar cells and modules through research and development" (KK.01.2.01.0115). M.T. L.B., and M.M. acknowledge the Central European Research Infrastructure Consortium(CERIC-ERIC) for the access to the SAXS beamline and related financial support (proposal number 20182085). The authors acknowledge Joško Erceg for assistance in the sample preparation and Dario Mičetić for the assistance during the GISAXS measurements.

References

[1] C. Cheng, Semiconductor Colloidal Quantum Dots for Photovoltaic Applications, PhD Thesis. University of Oxford, 2014.
[2] C. Summonte, M. Allegrezza, M. Bellettato, F. Liscio, M. Canino, A. Desalvo, J. López-vidrier, S. Hernández, L. López-conesa, S. Estradé, F. Peiró, B. Garrido, Silicon nanocrystals in carbide matrix, Sol. Energy Mater. Sol. Cells 128 (2014) 138–149, https://doi.org/10.1016/j.solmat.2014.05.003.
[3] S. Gutsch, J. Laube, A.M. Hartel, D. Hiller, N. Zakharov, P. Werner, M. Zacharias, Charge transport in Si nanocrystal/SiO2 superlattices, J. Appl. Phys. 133 (2013) 133703, https://doi.org/10.1063/1.4798395.
[4] C. Lin, H. Chen, Y.L. Tsai, H. Han, H. Shih, Y. Chang, H. Kuo, P. Yu, Highly efficient CdS quantum-dot-sensitized GaAs solar cells, Optic Express 20 (2012) 520–525, https://doi.org/10.1364/OE.20.00A319.
[5] F. Hetsch, X. Xu, H. Wang, S.V. Kershaw, A.L. Rogach, Semiconductor nanocrystal quantum dots as solar cell components and photosensitizers: material, charge transfer, and separation aspects of some device topologies, J. Phys. Chem. Lett. 2 (2011) 1879–1887, https://doi.org/10.1021/jz200802j.
[6] S. Saeed, C. De Weerd, P. Stallinga, F.C. Spoor, A.J. Houtepen, L.D.A. Siebbeles, T. Gregorkiewicz, Carrier multiplication in germanium nanocrystals, Light Sci. Appl. 4 (2015) 1–6, https://doi.org/10.1038/lsa.2015.24.

[7] M. Gordi, H. Ramezani, M.K. Moravvej-Farshi, Multiple exciton generation in Si and Ge nanocrystals: an ab initio comparative study, J. Phys. Chem. C 121 (2017) 6374–6379, https://doi.org/10.1021/acs.jpcc.7b00512.

[8] M.T. Trinh, R. Limpens, W.D.A.M. De Boer, J.M. Schins, L.D.A. Siebbeles, T. Gregorkiewicz, Direct generation of multiple excitons in adjacent silicon nanocrystals revealed by induced absorption, Nat. Photon. 6 (2012) 316–321, https://doi.org/10.1038/nphoton.2012.36.

[9] H. Goodwin, T.C. Jellicoe, N.J.L.K. Davis, M.L. Böhm, Multiple exciton generation in quantum dot-based solar cells, Nanophotonics 7 (2018) 111–126, https://doi.org/10.1515/nanoph-2017-0034.

[10] R. Bahariqushchi, R. Raciti, A.E. Kasapoğlu, E. Gür, M. Sezen, E. Kalay, S. Mirabella, A. Aydinli, Stress evolution of Ge nanocrystals in dielectric matrices, Nanotechnology 29 (2018) 185704, https://doi.org/10.1088/1361-6528/aaaffa.

[11] V. Saikiran, N. Manikanthababu, N.S. Rao, S.V.S.N. Rao, A.P. Pathak, Synthesis and characterization of Ge nanocrystals embedded in high-k dielectric, Adv. Mat. Lett. 7 (5) (2016) 957–963, https://doi.org/10.5185/amlett.2016.6403.

[12] Y.M. Niquet, G. Allan, C. Delerue, M. Lannoo, Quantum confinement in germanium nanocrystals, Appl. Phys. Lett. 77 (2000) 1182. https://aip.scitation.org/doi/10.1063/1.1289659.

[13] S. Das, R. Aluguri, S. Manna, R. Singha, A. Dhar, L. Pavesi, S.K. Ray, Optical and electrical properties of undoped and doped Ge nanocrystals, Nanoscale Res. Lett. 7 (2012) 1–11, https://doi.org/10.1186/1556-276X-7-143.

[14] E.B. Kaganovich, D.V. Korbutyak, Y.V. Kryuchenko, I.M. Kupchak, E.G. Manoilov, A.V. Sachenko, Exciton states and photoluminescence in Ge quantum dots, Nanotechnology 18 (2007) 295401, https://doi.org/10.1088/0957-4484/18/29/295401.

[15] D. Tahir, H.J. Kang, S. Tougaard, Electronic and optical properties of aluminum oxide before and after surface reduction by Ar^+ bombardment, At. Indones. 40 (2014) 63–67, https://doi.org/10.17146/aij.2014.273.

[16] S. Baldovino, A. Molle, M. Fanciulli, Influence of the oxidizing species on the Ge dangling bonds at the (100) Ge/GeO_2 interface, Appl. Phys. Lett. 96 (2010) 222110, https://doi.org/10.1063/1.3446839.

[17] F.S. Minaye Hashemi, S. Thombare, A.F.I. Morral, M.L. Brongersma, P.C. McIntyre, Effects of surface oxide formation on germanium nanowire band-edge photoluminescence, Appl. Phys. Lett. 102 (2013) 251122, https://doi.org/10.1063/1.4812334.

[18] M. Buljan, U.V. Desnica, M. Ivanda, N. Radić, P. Dubček, G. Dražić, K. Salamon, S. Bernstorff, V. Holý, Formation of three-dimensional quantum-dot superlattices in amorphous systems: experiments and Monte Carlo simulations, Phys. Rev. B Condens. Matter 79 (2009) 1–11, https://doi.org/10.1103/PhysRevB.79.035310.

[19] N. Nekić, I. Šarić, K. Salamon, L. Basioli, J. Sancho-Parramon, J. Grenzer, R. Hübner, S. Bernstorff, M. Petravić, M. Mičetić, Preparation of non-oxidized Ge quantum dot lattices in amorphous Al_2O_3, Si_3N_4 and SiC matrices, Nanotechnology 30 (2019) 335601, https://doi.org/10.1088/1361-6528/ab1d3c.

[20] M. Buljan, N. Radić, M. Ivanda, I. Bogdanović-Radović, M. Karlušić, J. Grenzer, S. Prucnal, G. Dražić, G. Pletikapić, V. Svetličić, M. Jerčinović, S. Bernstorff, V. Holý, Ge quantum dot lattices in Al_2O_3 multilayers, J. Nanoparticle Res. 15 (2013) 1485, https://doi.org/10.1007/s11051-013-1485-9.

[21] M. Buljan, N. Radić, S. Bernstorff, G. Dražić, I. Bogdanović-Radović, V. Holy, Grazing-incidence small-angle X-ray scattering: application to the study of quantum dot lattices, Acta Crystallogr. Sect. A Found. Crystallogr. 68 (2012) 124–138, https://doi.org/10.1107/S0108767311040104.

[22] S.R.C. Pinto, M. Buljan, A. Chahboun, M.A. Roldan, S. Bernstorff, M. Varela, S. J. Pennycook, N.P. Barradas, E. Alves, S.I. Molina, M.M.D. Ramos, M.J.M. Gomes, Tuning the properties of Ge-quantum dots superlattices in amorphous silica matrix through deposition conditions, J. Appl. Phys. 111 (2012), 074316, https://doi.org/10.1063/1.3702776.

[23] M. Buljan, U.V. Desnica, M. Ivanda, N. Radić, P. Dubček, G. Dražić, K. Salamon, S. Bernstorff, V. Holý, Formation of three-dimensional quantum-dot superlattices in amorphous systems: experiments and Monte Carlo simulations, Phys. Rev. B Condens. Matter 79 (2009) 1–11, https://doi.org/10.1103/PhysRevB.79.035310.

[24] E. Alfonso, J. Olaya, G. Cubillos, Thin film growth through sputtering technique and its applications, Crystallization–Science and Technology (2011) 397–432.

[25] M. Wen, C.Q. Hu, Q.N. Meng, Z.D. Zhao, T. An, Y.D. Su, W.X. Yu, W.T. Zheng, Effects of nitrogen flow rate on the preferred orientation and phase transition for niobium nitride films grown by direct current reactive magnetron sputtering, J. Phys. D Appl. Phys. 42 (2008) 35304, https://doi.org/10.1088/0022-3727/42/3/035304.

[26] G. Lu, L. Yu, H. Ju, B. Zuo, J. Xu, Influence of nitrogen content on the thermal diffusivity of TiN films prepared by magnetron sputtering, Surf. Eng. 36 (2020) 192–198, https://doi.org/10.1080/02670844.2019.1646964.

[27] I. Saric, R. Peter, M. Petravic, Oxidation of cobalt by oxygen bombardment at room temperature, J. Phys. Chem. C 120 (2016) 22421–22425, https://doi.org/10.1021/acs.jpcc.6b07139.

[28] T.N. Nunley, N.S. Fernando, N. Samarasingha, J.M. Moya, C.M. Nelson, A. Medina, S. Zollner, Optical constants of germanium and thermally grown germanium dioxide from 0.5 to 6.6eV via a multisample ellipsometry investigation, J. Vacuum. Sci. Technol B, Nanotechnol. Microelectronics: Mater. Process. Meas. Phenomena 34 (6) (2016), 061205, https://doi.org/10.1116/1.4963075.

[29] G. Cody, T. Tiedje, T.D. Moustakas, Y. Goldstein, Disorder and the optical-absorption edge of hydrogenated amorphous, J. Phys. Colloq. 42 (1981) C4-301–C4-304, https://doi.org/10.1051/jphyscol:1981463.

[30] S. Shi, S. Qian, X. Hou, J. Mu, J. He, X. Chou, Structural and optical properties of amorphous Al_2O_3 thin film deposited by atomic layer deposition, Adv. Condens. Matter Phys. (2018) 7598978, https://doi.org/10.1155/2018/7598978.

[31] M. Buljan, N. Radić, J. Sancho-Paramon, V. Janicki, J. Grenzer, I. Bogdanović-Radović, Z. Siketić, M. Ivanda, A. Utrobičić, R. Hübner, R. Weidauer, V. Valeš, J. Endres, T. Car, M. Jerčinović, J. Roško, S. Bernstorff, V. Holy, Production of three-dimensional quantum dot lattice of Ge/Si core-shell quantum dots and Si/Ge layers in an alumina glass matrix, Nanotechnology 26 (2015) 65602, https://doi.org/10.1088/0957-4484/26/6/065602.

[32] N. Nekić, J. Sancho-Parramon, I. Bogdanović-Radović, J. Grenzer, R. Hübner, S. Bernstorff, M. Ivanda, M. Buljan, Ge/Si core/shell quantum dots in alumina: tuning the optical absorption by the core and shell size, Nanophotonics 6 (2017) 1055–1062, https://doi.org/10.1515/nanoph-2016-0133.

[33] E.G. Barbagiovanni, D.J. Lockwood, P.J. Simpson, L.V. Goncharova, Quantum confinement in Si and Ge nanostructures: theory and experiment, Appl. Phys. Rev. 1 (2014), 011302, https://doi.org/10.1063/1.4835095.

[34] Q. Cai, H. Zhou, F. Lu, Enhanced infrared response of Si base p–n diode with self-assembled Ge quantum dots by thermal annealing, Appl. Surf. Sci. 254 (2008) 3376–3379, https://doi.org/10.1016/j.apsusc.2007.11.019.

[35] B. Filippone, C. Donaldson, M. Shayesteh, D. O'Connell, K. Huet, I. Toqué-Tresonne, F. Crupi, R. Duffya, Electrical characterization of the influence of the annealing energy density on carrier lifetimes in germanium, ECS Journal of Solid State Science and Technology 5 (2016) 3013–3017, https://doi.org/10.1149/2.0031604jss.

[36] A. Zekry, A. Yousef Al-Mazroo, A distributed SPICE-model of a solar cell, IEEE Trans. Electron. Dev. 43 (1996) 691–700, https://doi.org/10.1109/16.491244.